JGR Atmospheres

RESEARCH ARTICLE
10.1029/2024JD041022

Key Points:

- Flux convergence and divergence are caused by increasing variations in the magnitudes of sensible heat fluxes as the measurement height increases
- Vertical convergence and divergence in sensible heat fluxes are largely associated with variations in turbulent transport efficiency
- Variations in turbulent transport efficiency are caused by changes in asymmetric transport of updrafts and downdrafts

Correspondence to:
H. Liu,
heping.liu@wsu.edu

Citation:
Gao, Z., Li, L., Liu, H., & Yang, B. (2025). Flux convergence and divergence linked to asymmetric transport by large turbulent eddies in the unstable atmospheric surface layer. *Journal of Geophysical Research: Atmospheres*, *130*, e2024JD041022. https://doi.org/10.1029/2024JD041022

Received 18 FEB 2024
Accepted 7 DEC 2024

Flux Convergence and Divergence Linked to Asymmetric Transport by Large Turbulent Eddies in the Unstable Atmospheric Surface Layer

Zhongming Gao[1,2], Lei Li[1,2], Heping Liu[3], and Bai Yang[4]

[1]School of Atmospheric Sciences, Southern Marine Science and Engineering Guangdong Laboratory (Zhuhai), Sun Yat-sen University, Zhuhai, China, [2]Key Laboratory of Tropical Atmosphere-Ocean System, Ministry of Education, Sun Yat-sen University, Zhuhai, China, [3]Laboratory for Atmospheric Research, Department of Civil and Environmental Engineering, Washington State University, Washington, DC, USA, [4]Campbell Scientific, Inc., Logan, UT, USA

Abstract It is well-established that large eddies significantly influence the turbulent transport of heat and scalars in the atmospheric surface layer. However, the mechanistic understanding of how large eddies originating from both the ground (updrafts) and aloft (downdrafts) regulate flux convergence (FC) and divergence (FD) remains relatively unexplored. Based on turbulence data measured at 12 levels, spanning from 1.2 to 60.5 m above the ground, we observe a notable increase in the variability of sensible heat flux magnitudes with height. Our results show that FC and FD of sensible heat are primarily linked to variations in the respective transport efficiencies ($\gamma_{w\theta}$) at different heights. Using the cross-wavelet transform, we find that in FC cases, the regions with high wavelet coherence expand with height, resulting in higher $\gamma_{w\theta}$ at higher levels compared to low ones. Conversely, in FD cases, the regions with high wavelet coherence decrease with height, leading to lower $\gamma_{w\theta}$ at higher levels. Large eddies with length scales of approximately 120–500 m have a significant impact on amplifying or attenuating $\gamma_{w\theta}$ at higher levels compared to lower levels. Using conditional sampling to extract the updrafts and downdrafts of large eddies, distinct patterns are observed in the characteristics of updrafts and downdrafts between FC and FD groups especially in their flux contribution and transport efficiencies. This work emphasizes the significant contribution of asymmetric turbulent transport by updrafts and downdrafts to the discrepancy between the observed turbulent fluxes and those predicted by the Monin-Obukhov similarity theory.

Plain Language Summary Large eddies play an important role in modulating the turbulent transport of heat and scalars within the atmosphere close to the surface. This study explores how updrafts (originating from the ground) and downdrafts (descending from above) of large eddies affect the vertical convergence and divergence of sensible heat fluxes. We analyze turbulent data collected at 12 different levels up to a height of 60.5 m above the ground. Our findings indicate that variations in turbulent transport efficiencies at various levels associate with the observed differences in flux divergence and convergence. These differences are primarily driven by large eddies with length scales of several hundred meters. Specifically, when flux convergence occurs, there is an increase in areas with similar power as height increases, leading to more efficient turbulent transport at higher levels compared to lower ones. On the other hand, during flux divergence, a decrease in regions with common power at higher altitudes results in reduced transport efficiency. These findings suggest that the asymmetric transport behavior between updrafts and downdrafts significantly affects heat fluxes, deviating from predictions based on classical Monin-Obukhov similarity theory.

1. Introduction

Over the past several decades, extensive attention has been directed toward understanding the turbulent transport of heat, water vapor, and other scalars (e.g., carbon dioxide and methane) in the atmospheric surface layer (ASL) primarily due to its importance in assessing the surface energy budget and ecosystem water and carbon cycles (Dupont & Patton, 2012; Z. Gao et al., 2017; Katul et al., 1997; D. Li & Bou-Zeid, 2011; D. Li et al., 2018; Sun et al., 2016; G. Wang et al., 2010; L. Wang et al., 2014; Yao et al., 2020). Here, we define the ASL as the bottom few decameters of the atmospheric boundary layer (Stull, 1988; Sun et al., 2016). In the ASL, turbulence is characterized by multiple scales of motions that are superimposed on each other (Stull, 1988). Notably, low-frequency large-scale coherent motions, or large eddies, are crucial for regulating turbulent transfer processes within the ASL (Foken, 2008; Z. Gao et al., 2017; Liu et al., 2021; McNaughton & Laubach, 2000;

Ruppert et al., 2006; Smedman et al., 2007; Y. Zhang et al., 2010, 2011). These large eddies are responsible for the dissimilarity of turbulent scalar transport of heat and water vapor especially those large eddies with frequencies below around 0.01 Hz (Ruppert et al., 2006). Moreover, large eddies are recognized for causing discrepancies between observed features and the predictions of Monin-Obukhov similarity theory (MOST) (Andreas, 1987; McNaughton & Laubach, 2000; Ruppert et al., 2006; Smedman et al., 2007; Sun et al., 2016; Y. Zhang et al., 2010). Therefore, understanding the impact of large eddies on turbulent transport is crucial for research on land-atmosphere interaction, water and carbon cycling, and air quality management.

Previous studies have indicated that large eddies can significantly alter turbulent fluxes (Eder et al., 2015; Z. Gao et al., 2017; Stoy et al., 2013; Zhou et al., 2018). However, the precise contribution of large eddies to turbulent fluxes can vary due to factors such as atmospheric stability (Barthlott et al., 2007; Thomas & Foken, 2007). Atmospheric instability modifies the characteristics of large eddies (Steiner et al., 2011). With increasing instability, shear-driven large eddies, such as hairpin vortices and packets, are progressively replaced by buoyancy-driven motions, such as thermals and plumes (Dupont & Patton, 2012; D. Li & Bou-Zeid, 2011; L. Zhang et al., 2023), leading to changes in the scalar transport efficiency (D. Li & Bou-Zeid, 2011). Such large eddies can either enhance or suppress turbulent fluxes differently at different heights, leading to flux convergence (FC, larger fluxes at higher levels) and divergence (FD, lower fluxes at higher levels) in the vertical direction (Z. Gao et al., 2016; Y. Zhang et al., 2010).

During daytime unstable conditions, large eddies can be further categorized as updrafts that are generated from the heated surface and ascend and downdrafts that are produced from the well-mixed layer aloft and descend, leading the ASL's interaction and coupling with the overlying mixed layer (D. Li et al., 2018; Liu et al., 2021; Stull, 1988). Downdrafts follow the mixed-layer scaling and lead to the failures of the Monin-Obukhov similarity theory (MOST) under strongly unstable conditions, whereas updrafts can be reasonably predicted by the MOST (Q. Li et al., 2018). Asymmetric turbulent transport of heat and water vapor by updrafts and downdrafts of large eddies under unstable ASL conditions causes a reduction in fluxes (Liu et al., 2021). Recent studies also indicate that such large eddies can enlarge phase differences between low-frequency signals of vertical velocity and scalars, leading to a decrease in scalar transport efficiency and thus turbulent fluxes (Z. Gao et al., 2017). Despite the already recognized roles of downdrafts and updrafts of large eddies in turbulent transport, linking these processes to the substantial variations in turbulent fluxes with height (i.e., FC and FD) remains a lesser-studied area.

Therefore, the objectives of this study are (a) to investigate the causes for the generally observed large variations in sensible heat fluxes and (b) to examine the role of updrafts and downdrafts of large eddies in vertical flux convergence and divergence. The turbulence data collected by multiple levels of eddy covariance systems and sonic anemometers up to 60 m above the ground, as part of the field experiment of turbulence measurements over heterogeneous landscapes, are analyzed to address these objectives. Section 2 describes the site of the experiment, the data, and the methodologies used in this study. Section 3 presents the results and discussion, and Section 4 summarizes the conclusions.

2. Materials and Methods

2.1. Experiment and Data

The data used in this study were obtained from an experiment on turbulence measurements over heterogeneous landscapes conducted in southeastern Idaho, USA (43.59°N, 112.94°W; 1,500 m above mean sea level; Figure 1). The time zone is Mountain Standard Time (MST = UTC – 7; where UTC is Coordinated Universal Time). The study site is located on a broad relatively flat plain on the western edge of the Snake River Plain. A comprehensive description of this site is documented elsewhere (Finn et al., 2016, 2018). Briefly, the prevailing wind directions during daytime and nighttime are southwest and northeast, respectively. A 62 m tower, located about 13 km southeast of the nearest mountains, provides vertical profile measurements of air temperature, wind speed and wind direction, turbulence, and fluxes. Shrubs and grasses in the site are relatively uniform. Based on the wind profiles measured from the 62 m tower, the roughness lengths are estimated to be approximately 3.0 and 3.8 cm for the prevailing winds of the southwest and northeast, respectively, whereas the estimated displacement height is not significantly different from zero (Finn et al., 2016).

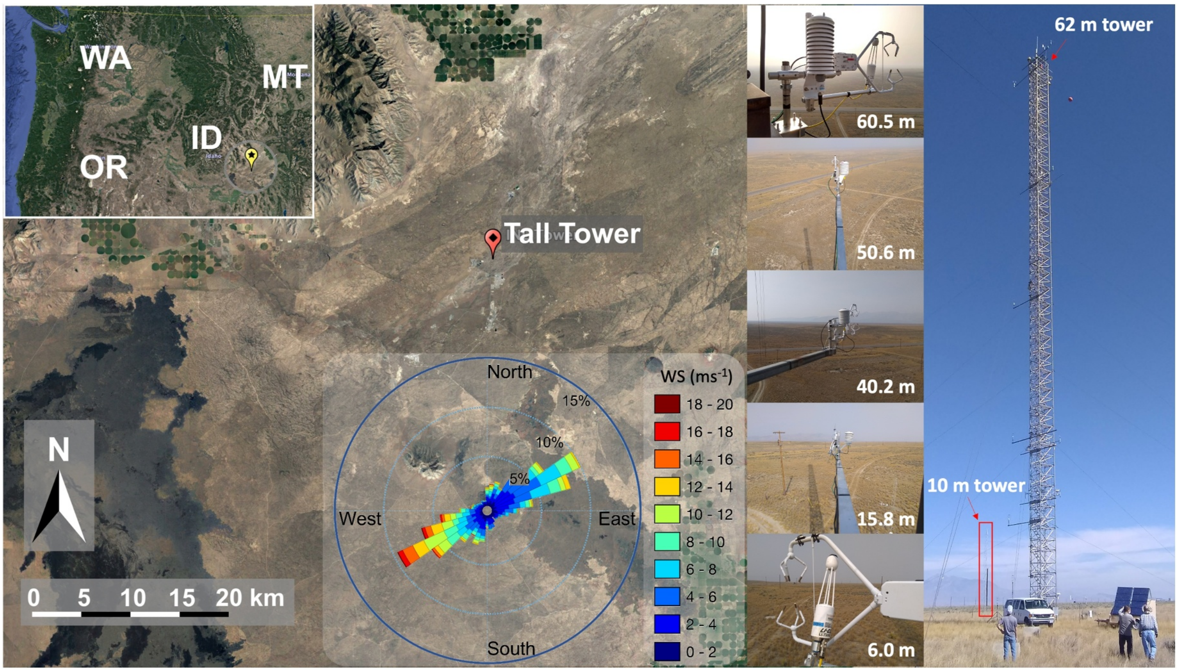

Figure 1. Google Earth images showing the site in southeastern Idaho, United States, and photos of the towers and some of the instruments deployed during the experiment. A wind rose displays the frequency of wind speeds and wind directions at the site.

During the experiment, a 10-m tower was erected about 15 m northwest of the 62-m tall tower (Z. Gao, Liu, et al., 2024). A variety of instruments were installed on both towers, including 12 sonic anemometers, 8 infrared gas analyzers, 12 temperature and relative humidity probes, and one net radiometer. The 62-m tower accommodated eight levels of the eddy covariance systems, whereas the 10-m tower hosted four levels. The 3D sonic anemometers (Model CSAT3B/CSAT3, Campbell Scientific, Inc.) at heights of 1.2, 2.0, 3.5, 6.0, 8.2, 12.8, 15.8, 23.0, 30.3, 40.2, 50.6, and 60.5 m measured the components of the three-dimensional wind velocity (u, v, and w) and the sonic air temperature (θ). The infrared gas analyzer (Model LI7500RS/LI7500A/LI7500, LICOR, Inc.) at heights of 1.2, 2.0, 6.0, 12.8, 23.0, 30.3, 40.2, and 60.5 m measured the densities of water vapor and CO_2. Both the sonic anemometers and gas analyzers were sampled at 10 Hz using three dataloggers (Model CR1000X, Campbell Scientific, Inc.), while the rest of the low-frequency instruments were sampled at 0.2 Hz. To ensure simultaneous operation of the three dataloggers, three GPS receivers (Model GPS16X-HVS, Garmin International, Inc.) were utilized for clock synchronization. The measurements collected during 20 September to 31 December 2020 are analyzed in this study.

2.2. Post-Field Data Processing and Data Selection

In this study, turbulent fluxes of momentum, sensible (H), and latent (LE) heat were computed in 30-min intervals using standard post-field data processing procedures (Z. Gao et al., 2016; Mauder et al., 2007; Y. Zhang et al., 2010) with an update on the sequence of density effect corrections (Z. Gao et al., 2020). Briefly, the raw 10-Hz data were filtered for instrument failures and physically implausible values. Next, despiking was performed (Vickers & Mahrt, 1997). The 3D wind components of u, v, and w were rotated according to the planar fit method (Wilczak et al., 2001). Fluctuating parts of sonic temperature and water vapor density related to their time-averaged means were adjusted iteratively to account for the effects of specific humidity (Liu et al., 2001; Schotanus et al., 1983) and air density fluctuations (Detto & Katul, 2007; Z. Gao et al., 2020; Webb et al., 1980). Subsequently, fluxes were calculated as the covariances of the corrected fluctuations of the vertical wind component (w) and the corresponding variables (u, θ, and q) for each 30-min interval. For statistical analysis, data were selected based on the following criteria: (a) the Obukhov stability parameter, z/L, was less than zero to define unstable conditions; (b) the turbulence intensity, $\sigma_u/\overline{u}$, was less than 0.5 to ensure compliance with Taylor's turbulence hypothesis; (c) the net radiation and sensible heat flux were larger than 50 W m^{-2} and 10 W m^{-2}, respectively, to ensure a relatively well-developed convective boundary layer and a meaningful results.

2.3. Wavelet Analysis

Wavelet analysis, encompassing the continuous wavelet transform and the cross-wavelet transform, has emerged as a valuable tool for studying the ASL turbulence (Farge, 1992; W. Gao & Li, 1993; Z. Gao et al., 2016; Hudgins et al., 1993; Katul et al., 2001; Lan et al., 2018). Unlike the Fourier transform, wavelet analysis can effectively handle nonstationary transition periods of turbulence observations (Z. Gao et al., 2016; Hudgins et al., 1993). The continuous wavelet transform allows the expansion of a time series into a time-frequency space, providing insights into the temporal and spatial scales of large eddies. On the other hand, the cross-wavelet transform facilitates the identification of regions with high common power between two time series and reveals information about their phase relationship (Grinsted et al., 2004).

The continuous wavelet transform of a time series x_t is defined as

$$W_n^x(s) = \sqrt{\frac{\delta t}{s}} \sum_{t=0}^{N-1} x_t \psi_0 \left[\frac{(t-n)\delta t}{s}\right], \tag{1}$$

where ψ_0 denotes a scaled and translated wavelet function, n is the localized time index, N is the number of points, and $\sqrt{\delta t/s}$ is used to normalize the wavelet function at each wavelet scale s. The cross-wavelet transform of two time series x_t and y_t is defined as

$$W_n^{xy}(s) = W_n^x W_n^{y*}, \tag{2}$$

where * denotes the complex conjugation. The phase angle and wavelet coherence of two time series are obtained as

$$\Phi(s) = \tan^{-1}\left(\frac{Im\left(W_n^{xy}(s)\right)}{Re\left(W_n^{xy}(s)\right)}\right), \tag{3}$$

$$R_n^2(s) = \frac{\left|S\left(s^{-1}W_n^{xy}(s)\right)\right|^2}{\left|S\left(s^{-1}W_n^{x}(s)\right)\right|^2 \left|S\left(s^{-1}W_n^{x}(s)\right)\right|^2}, \tag{4}$$

where Im and Re denote the imaginary and real parts of the cross wavelet transform, respectively, and S is a smoothing operator.

3. Results and Discussion

3.1. The Increased Varying Magnitudes of the Sensible Heat Flux With Height Leading to Changes in Flux Convergence and Divergence

Figure 2 illustrates the diurnal variations of H, z/L, friction velocity $\left(u_* = \sqrt[1/4]{\overline{u'w'^2} + \overline{v'w'^2}}\right)$, turbulent kinetic energy $\left(\mathrm{TKE} = 0.5\left(\overline{u'^2 + v'^2 + w'^2}\right)\right)$, wind speed, the transport efficiency for $\overline{w'\theta'}$ ($\gamma_{w\theta}$, defined as the correlation coefficient between w' and θ' with larger magnitudes of $\gamma_{w\theta}$ indicating enhanced transport efficiencies), and the product of standard deviations of w and θ ($\sigma_w * \sigma_\theta$) observed at different levels from 1.2 m up to 60.5 m during September 29 to 2 October 2020. Note that, for the variables of H, z/L, $\gamma_{w\theta}$ and $\sigma_w * \sigma_\theta$, only the levels with the availability of both a 3D sonic anemometer and an infrared gas analyzer are shown here because the density of water vapor is needed to determine H.

Under unstable ASL conditions (e.g., 10:30–15:30), although the net radiation (R_n) follows a smoothed sine pattern on cloudless days, the half-hourly H exhibits large point-to-point variations particularly more pronouncing at higher levels than at lower levels (Figure 2a). For instance, H at 60.5 m increases by approximately 236 W m^{-2} from 12:30 to 13:00 MST on September 29, whereas H at 1.2 m increases by only about 25 W m^{-2}. The increasing variations in the magnitudes of sensible heat fluxes at higher levels result in changes in FC and FD. The observed diverse patterns between H and R_n suggest that factors beyond surface heating exert a substantial influence on the large variations in H, thereby inducing distinct alterations in H at different heights. Similar features with ideal

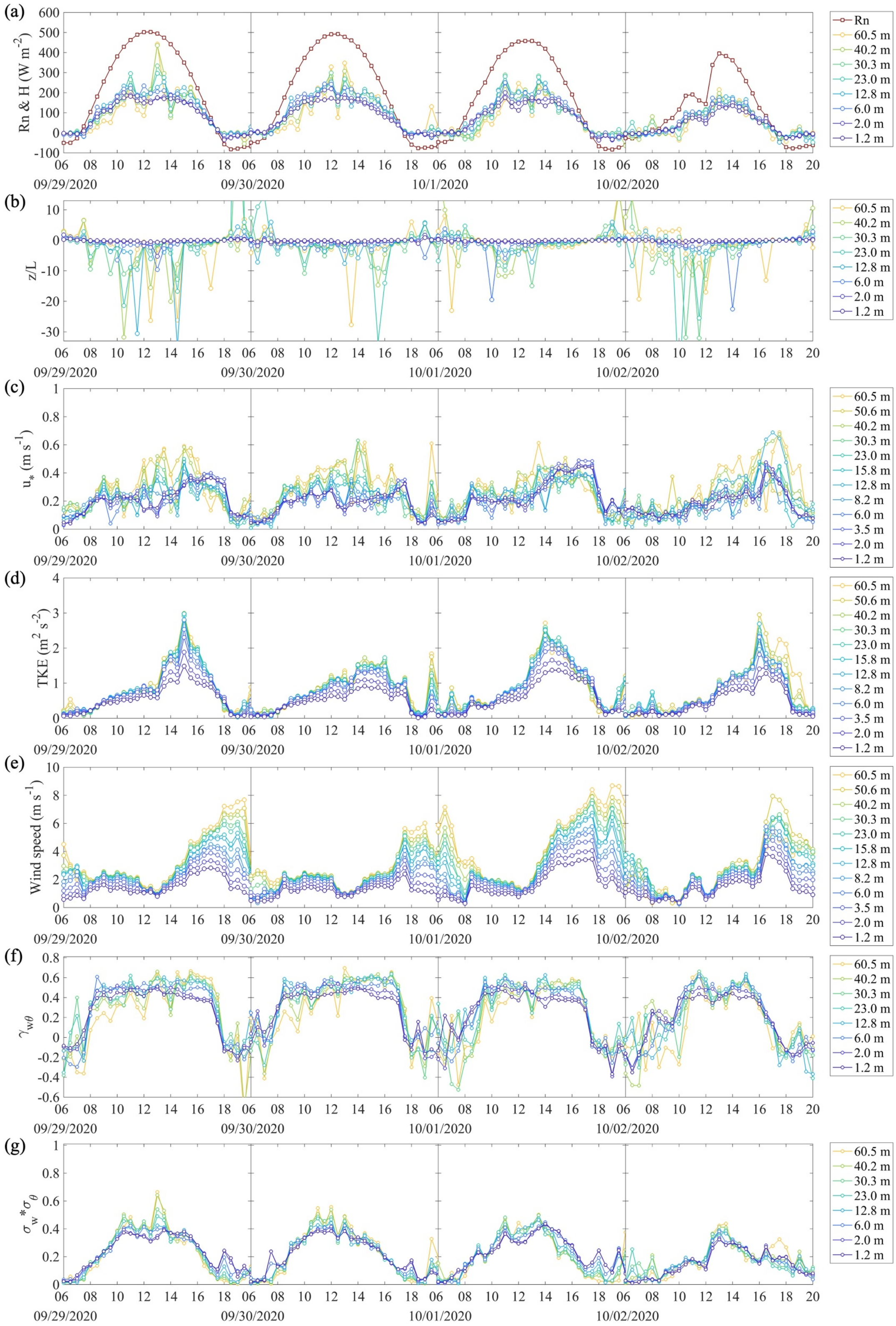

Figure 2. Diurnal variations of (a) net radiation (Rn) and sensible heat flux (H), (b) stability parameter (z/L), (c) friction velocity (u_*), (d) turbulent kinetic energy (TKE), (e) wind speed, (f) the transport efficiency for $\overline{w'\theta'}$ ($\gamma_{w\theta}$, defined as the correlation coefficient between w' and θ'), and (g) the product of standard deviations of w and θ ($\sigma_w * \sigma_\theta$) at different levels during 29 September to 2 October 2020. R_n is the net radiation measured at 40.2 m.

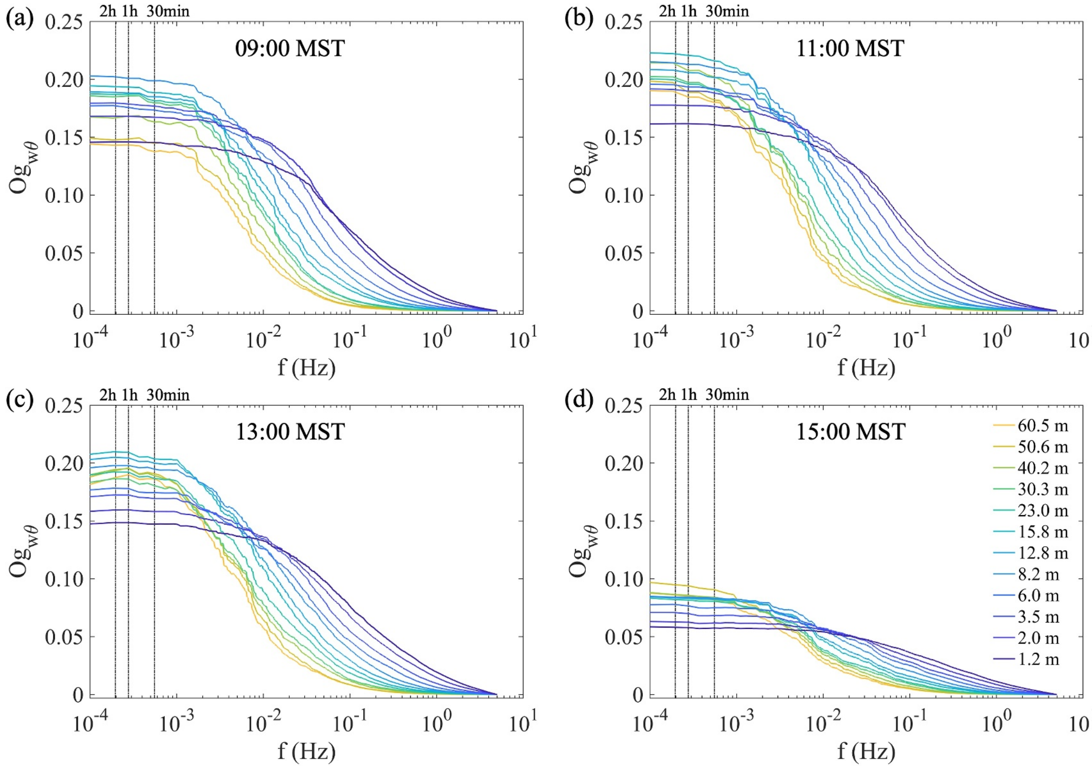

Figure 3. The Ogive function of w-θ at 12 heights for four selected 3-hr intervals starting at (a) 09:00, (b) 11:00, (c) 13:00, and (d) 15:00 MST, respectively, on 29 September 2020. The three dashed lines represent time durations of 30-min, 1 hr, and 2 hr from left to right, respectively.

sine-shaped R_n but largely varying latent heat fluxes have been observed at other sites in previous studies (Z. Gao et al., 2016; Y. Zhang et al., 2010), and a general explanation is that nonlocal processes (e.g., large eddies) can either enhance or suppress the turbulent fluxes in the ASL.

In addition to H, during the unstable daytime conditions, significant point-to-point variations are also observed in z/L and u_* at various heights (Figures 2b and 2c). Moreover, TKE exhibits a gradual increase in the morning, reaching its peak in the early afternoon before subsequently decreasing (Figure 2d). These results suggest that factors influencing H also have a significant influence on momentum fluxes, while having no discernible impact on the standard deviations of wind velocity components (Högström, 1990). However, the dissimilarity in turbulent transport of momentum and scalars has been extensively documented in the unstable ASL (e.g., D. Li & Bou-Zeid, 2011). Therefore, our main emphasis is placed on examining the fundamental factors that contribute to the convergence and divergence of sensible heat fluxes. As shown in Figure 2f, the variations of $\gamma_{w\theta}$ demonstrate a comparable pattern to that observed for H during the daytime. For instance, at 13:00 MST on September 29, higher levels display larger $\gamma_{w\theta}$ values, coinciding with higher H at those levels, whereas at 14:00 MST, higher levels show relatively smaller $\gamma_{w\theta}$ values, corresponding to lower H at those levels. The synchronous varying patterns of H and $\gamma_{w\theta}$ suggest that the mechanism responsible for the increased varying magnitudes of H with height also results in improved or degraded $\gamma_{w\theta}$, although variations in the magnitudes of $\sigma_w * \sigma_\theta$ also contribute to changes in H (Figure 2e; Z. Gao et al., 2017).

Ogive analysis is also utilized to investigate whether a 30-min averaging time length is sufficient to capture all turbulent motions and their flux contributions to H especially at higher levels (Charuchittipan et al., 2014). Four 3-hr intervals, starting at 09:00, 11:00, 13:00, and 15:00 on 29 September 2020, respectively, are analyzed with the data obtained from all 12 levels. We emphasize that we confirm the strong representativeness of these four intervals with respect to vertical variations in fluxes at different heights. As can be seen from Figure 3, extending the averaging time from 30 min to as long as 3 hr does not lead to an increase in $\overline{w'\theta'}$ at both heights of 60.5 and 50.6 m. These results indicate that the lower H observed at the height of 60.5, in comparison to other heights in Figure 2a, is not attributed to inadequate averaging time. Finn et al. (2016) reported that the mixing-layer height

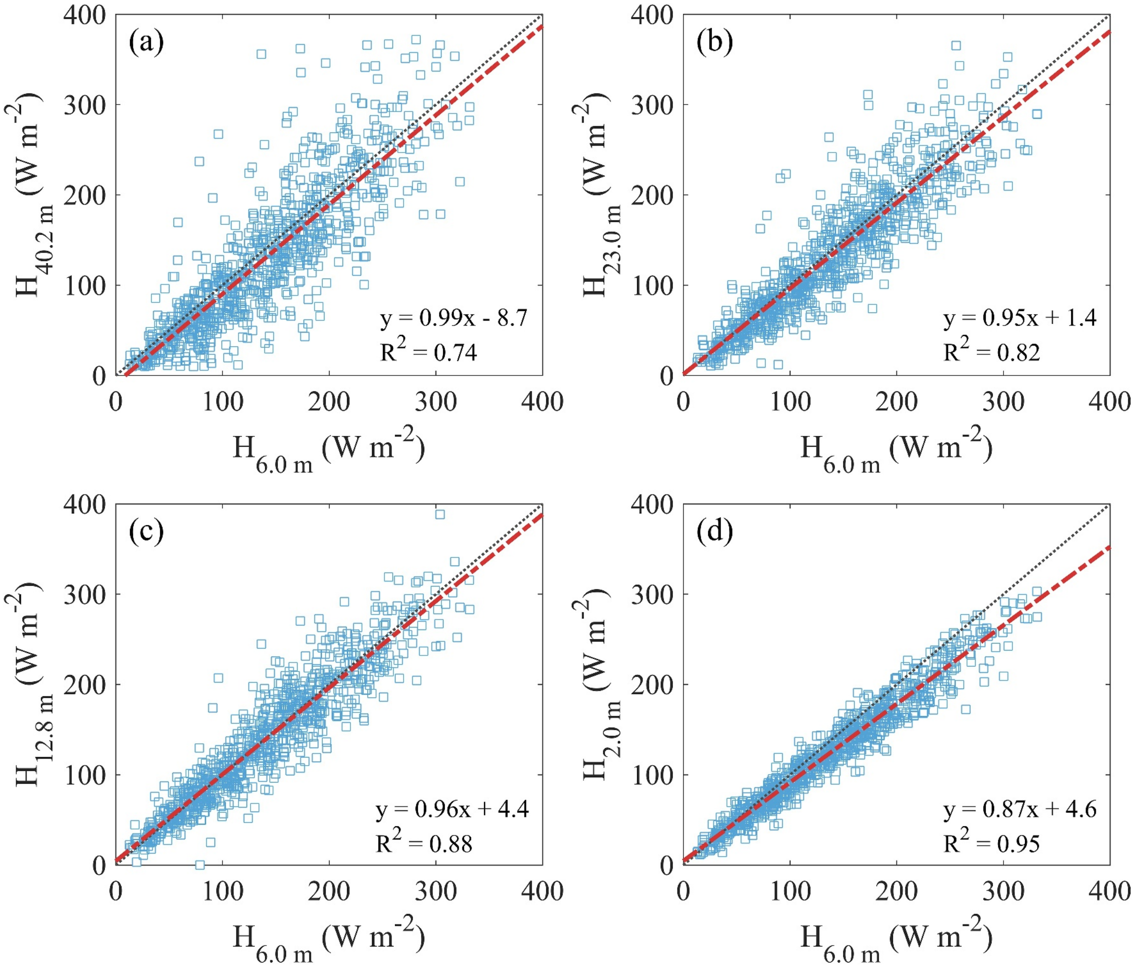

Figure 4. Scatter plots of the half-hourly sensible heat flux (*H*) at (a) 40.2 m, (b) 23.0 m, (c) 12.8 m, and (d) 2.0 m versus *H* at 6.0 m, respectively. Red and black dashed lines denote linear regression and 1:1 line, respectively.

during early afternoon in October 2013 varied from approximately 950 m to around 2,100 m as determined by potential temperature data obtained from radiosonde soundings. Therefore, we expect a lower but rapidly developing mixing-layer in the morning, resulting in the decorrelation between w and θ (Figure 2f) and thus lower H than other heights. Furthermore, the magnitudes of the Obukhov length vary within several decameters (not shown here), indicating that measurements at higher levels may fall outside the constant flux layer during the morning. Additionally, it is also noted that the ogive function of w-θ consistently display lower values at the height of 1.2 m compared to most other heights regardless of the length of the averaging time, suggesting that the measurements at lower levels are influenced by the roughness sublayer.

3.2. Flux Divergence and Convergence Linked to Changes in Turbulent Transport Efficiency

Although the linear regressions of sensible heat fluxes at 6.0 m compared to other heights closely align with the 1:1 line, their distributions become more scattered as the measurement height increases (Figure 4). The R^2 between H at 6.0 and 2.0 m is 0.95, while it decreases to 0.74 for between H at 40.2 and 6.0 m. H at higher levels and 6.0 m exhibits a strong linear regression close to 1, indicating the absence of any systematic underestimation or overestimation across these levels. Note that the linear regression between H at 2.0 and 6.0 m has a slope of 0.87, indicating that the measurement of H at 2.0 m is also underestimated, aligning with the findings from the ogive analysis. These features indicate the presence of significant FC and FD at the study site under unstable conditions. The magnitudes of FC and FD are more pronounced between the higher level and 6.0 m. Therefore, in the subsequent sections, we focus our investigation on the data at the two levels of 40.2 and 6.0 m.

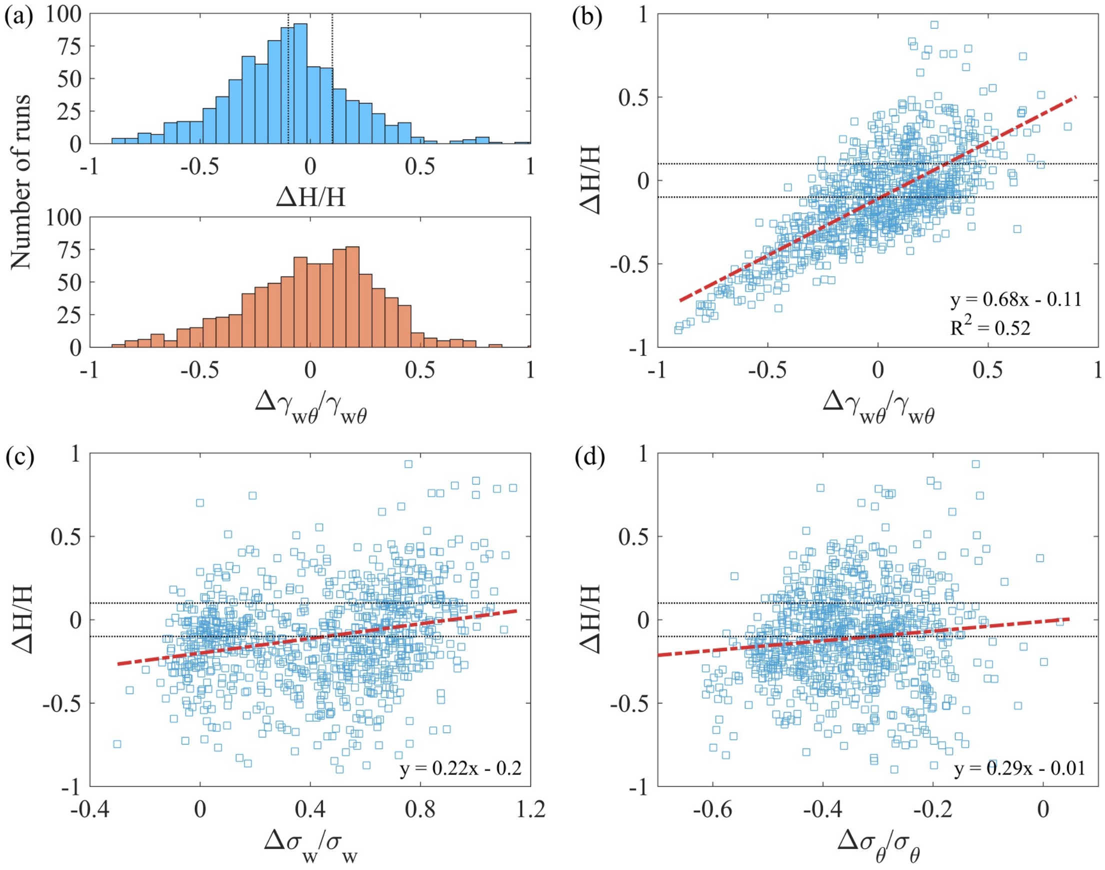

Figure 5. (a) Histograms of relative changes in sensible heat fluxes $\left(\frac{\Delta H}{H}\right)$ and transport efficiency $\left(\frac{\Delta \gamma_{w\theta}}{\gamma_{w\theta}}\right)$ between 40.2 and 6.0 m and scatter plots of $\frac{\Delta H}{H}$ vs. (b) $\frac{\Delta \gamma_{w\theta}}{\gamma_{w\theta}}$ and relative changes in standard deviation for (c) vertical velocity $\left(\frac{\Delta \sigma_w}{\sigma_w}\right)$ and (d) air temperature $\left(\frac{\Delta \sigma_\theta}{\sigma_\theta}\right)$ between 40.2 and 6.0 m. The red dashed line denotes the linear regression. The black dashed lines denote the ±10% of $\frac{\Delta H}{H}$.

The transport efficiency for $\overline{w'\theta'}$ provides a means to investigate the key factors influencing the flux divergence and convergence of H. By employing the following equation derived from $\gamma_{w\theta} = \overline{w'\theta'}/\sigma_w\sigma_\theta$ (Lan et al., 2018), we quantify the relative contributions of different terms to the increased varying magnitudes of $\overline{w'\theta'}$ with height and consequently H:

$$\frac{\Delta H}{H} \equiv \frac{\Delta \overline{w'\theta'}}{\overline{w'\theta'}} \approx \frac{\Delta \gamma_{w\theta}}{\gamma_{w\theta}} + \frac{\Delta \sigma_w}{\sigma_w} + \frac{\Delta \sigma_\theta}{\sigma_\theta} \tag{5}$$

where $\frac{\Delta H}{H}$, $\frac{\Delta \overline{w'\theta'}}{\overline{w'\theta'}}$, $\frac{\Delta \gamma_{w\theta}}{\gamma_{w\theta}}$, $\frac{\Delta \sigma_w}{\sigma_w}$, and $\frac{\Delta \sigma_\theta}{\sigma_\theta}$ refer to the relative changes in H, kinematic heat flux, transport efficiency, standard deviation of w, and standard deviation of θ, respectively. Other high-order terms on the right side of Equation 5 are omitted. Here, the relative changes in these terms are calculated as the difference of the corresponding terms between 40.2 and 6.0 m divided by the value at 6.0 m. For instance, $\frac{\Delta H}{H}$ is calculated as $(H_{40.2\ \mathrm{m}} - H_{6.0\ \mathrm{m}})/H_{6.0\ \mathrm{m}}$.

Figure 5 reveals a significant increase in $\frac{\Delta H}{H}$ with the increase in $\frac{\Delta \gamma_{w\theta}}{\gamma_{w\theta}}$ ($y = 0.68x - 0.11$; $R^2 = 0.52$; $P < 0.0001$), whereas $\frac{\Delta H}{H}$ experiences only a slight increase as both $\frac{\Delta \sigma_w}{\sigma_w}$ and $\frac{\Delta \sigma_\theta}{\sigma_\theta}$ increase. This result confirms that the large FC or FD are primarily associated with the enhancement or suppression of $\gamma_{w\theta}$ at higher levels compared to lower levels within the unstable ASL as demonstrated earlier in Figure 2. Between 40.2 and 6.0 m, $\frac{\Delta H}{H}$ ranged from -1.0 to around 1.0 with the peak number of occurrences close to 0.05, whereas $\frac{\Delta \gamma_{w\theta}}{\gamma_{w\theta}}$ ranged from -1.0 to around 1.0

with the highest number of runs around 0.3. The positively skewed distribution of $\frac{\Delta\gamma_{w\theta}}{\gamma_{w\theta}}$ suggests that turbulent transfer at higher levels is generally more efficient than that at lower levels in the unstable ASL.

Regarding $\frac{\Delta\sigma_w}{\sigma_w}$ and $\frac{\Delta\sigma_\theta}{\sigma_\theta}$, two features are noted: (a) $\frac{\Delta\sigma_w}{\sigma_w}$ varies from around −0.1 to 1.2, and $\frac{\Delta\sigma_\theta}{\sigma_\theta}$ varies from around −0.6 to zero, indicating that σ_w and σ_θ generally increase and decrease with height, respectively; (b) the increased magnitudes of σ_w from 6.0 to 40.2 m are larger than the decreased magnitudes of σ_θ. Both σ_w and σ_θ equally contribute to the variations in $\gamma_{w\theta}$, and the increased magnitudes of σ_w are almost twice of the decreased magnitudes of σ_θ from 6.0 to 40.2 m, leading to a larger turbulent transport efficiency for $\overline{w'\theta'}$ at higher levels. The mostly positive values of $\frac{\Delta\sigma_w}{\sigma_w}$ and negative values of $\frac{\Delta\sigma_\theta}{\sigma_\theta}$ also partially explains why $\frac{\Delta\sigma_w}{\sigma_w}$ and $\frac{\Delta\sigma_\theta}{\sigma_\theta}$ are not significantly related to $\frac{\Delta H}{H}$. Therefore, the significant convergence and divergence of H are primarily linked to variations in $\gamma_{w\theta}$.

3.3. Influence of Atmospheric Stability and Friction Velocity on Changes in Turbulent Transport Efficiency

Examining the controlling factors for changes in turbulent transport efficiency across layers can illustrate the role of different parameters in regulating the FC and FD in the ASL. To ensure the meaningfulness of the results, we classify the data as cases of FC when $\frac{\Delta H}{H} > 10\%$ and as cases of FD when $\frac{\Delta H}{H} < -10\%$, respectively. The number of runs belonging to FC and FD accounts for approximately 25% and 55% of the selected runs, respectively (Figure 5a). Figure 6 shows the distributions of $\frac{\Delta\gamma_{w\theta}}{\gamma_{w\theta}}$, $\frac{\Delta\sigma_w}{\sigma_w}$, and $\frac{\Delta\sigma_\theta}{\sigma_\theta}$ for FC and FD with increasing instability and friction velocity, respectively. As the instability increases from near-neutral to strongly unstable conditions, $\frac{\Delta\gamma_{w\theta}}{\gamma_{w\theta}}$ decreases from around 0.5 to zero with a slope of −0.2 for the cases of FC, whereas for the cases of FD, $\frac{\Delta\gamma_{w\theta}}{\gamma_{w\theta}}$ decreases from around zero to −0.4 with a slope of −0.15. In contrast, as the friction velocity increases, $\frac{\Delta\gamma_{w\theta}}{\gamma_{w\theta}}$ increases from around zero to 0.5 with a slope of 0.6 for FC, whereas for FD, $\frac{\Delta\gamma_{w\theta}}{\gamma_{w\theta}}$ increases from around −0.4 to zero with a slope of 0.51. Therefore, both atmospheric instability and friction velocity play important roles in regulating the vertical gradient of turbulent transport efficiencies. Note that the scattered distribution of $\frac{\Delta\gamma_{w\theta}}{\gamma_{w\theta}}$ under near-neutral conditions is primarily attributed to the data with friction velocities ranging from 0.5 to 0.9 m s^{-1} rather than the highest friction velocities (Figures 6a and 6b).

For FC and FD, we also observe certain differences in the varying trends of $\frac{\Delta\sigma_w}{\sigma_w}$ and $\frac{\Delta\sigma_\theta}{\sigma_\theta}$ with respect to |z/L| and u_* as well. As the instability increases, $\frac{\Delta\sigma_w}{\sigma_w}$ increases from around zero to 1.0 (Figure 6c), whereas $\frac{\Delta\sigma_\theta}{\sigma_\theta}$ decreases from −0.2 to around −0.5 for both FC and FD (Figure 6e). The magnitudes of the increasing trends in $\frac{\Delta\sigma_w}{\sigma_w}$ are greater than those of the decreasing trends in $\frac{\Delta\sigma_\theta}{\sigma_\theta}$ as |z/L| increases for both FC and FD. Conversely, as u_* increases, the magnitudes of the decreasing trends in $\frac{\Delta\sigma_w}{\sigma_w}$ are greater than those of the increasing trends in $\frac{\Delta\sigma_\theta}{\sigma_\theta}$ for FC and FD. Another notable feature is that the magnitudes of $\frac{\Delta\sigma_w}{\sigma_w}$ for the cases of FC are slightly greater compared to those for FD under unstable conditions with 0.1 < |z/L| < 10, which corresponded to conditions where $u_* < 0.5$ (Figure 6d). Overall, under unstable conditions of |z/L| < 0.1, when the vertical gradients in σ_w and σ_θ are constrained, FC is observed when $\gamma_{w\theta}$ at high levels is significantly larger than that at lower levels. However, as the gradients in σ_w further increase with enhanced instability, FC is observed even when $\gamma_{w\theta}$ at high levels is only slightly larger than that at lower levels.

3.4. Changes in Turbulent Transport Efficiency Related to Changes in Turbulence Structures

In coupled or well-mixed ASL, higher cross-layer correlations are expected to occur, as different levels experience the same turbulent eddies on vertical scales comparable to the measurement heights. However, the large difference in $\gamma_{w\theta}$ between 40.2 and 6.0 m indicates that different turbulent eddies are dominating the turbulent transport at these levels. To illustrate how different turbulent eddies influence the $\gamma_{w\theta}$, we employ the cross-wavelet transform to analyze the time series of turbulence fluctuation (i.e., w' and θ') for cases of FC and FD, respectively. The cross-wavelet transform enables for simultaneous identification of areas with a high localized

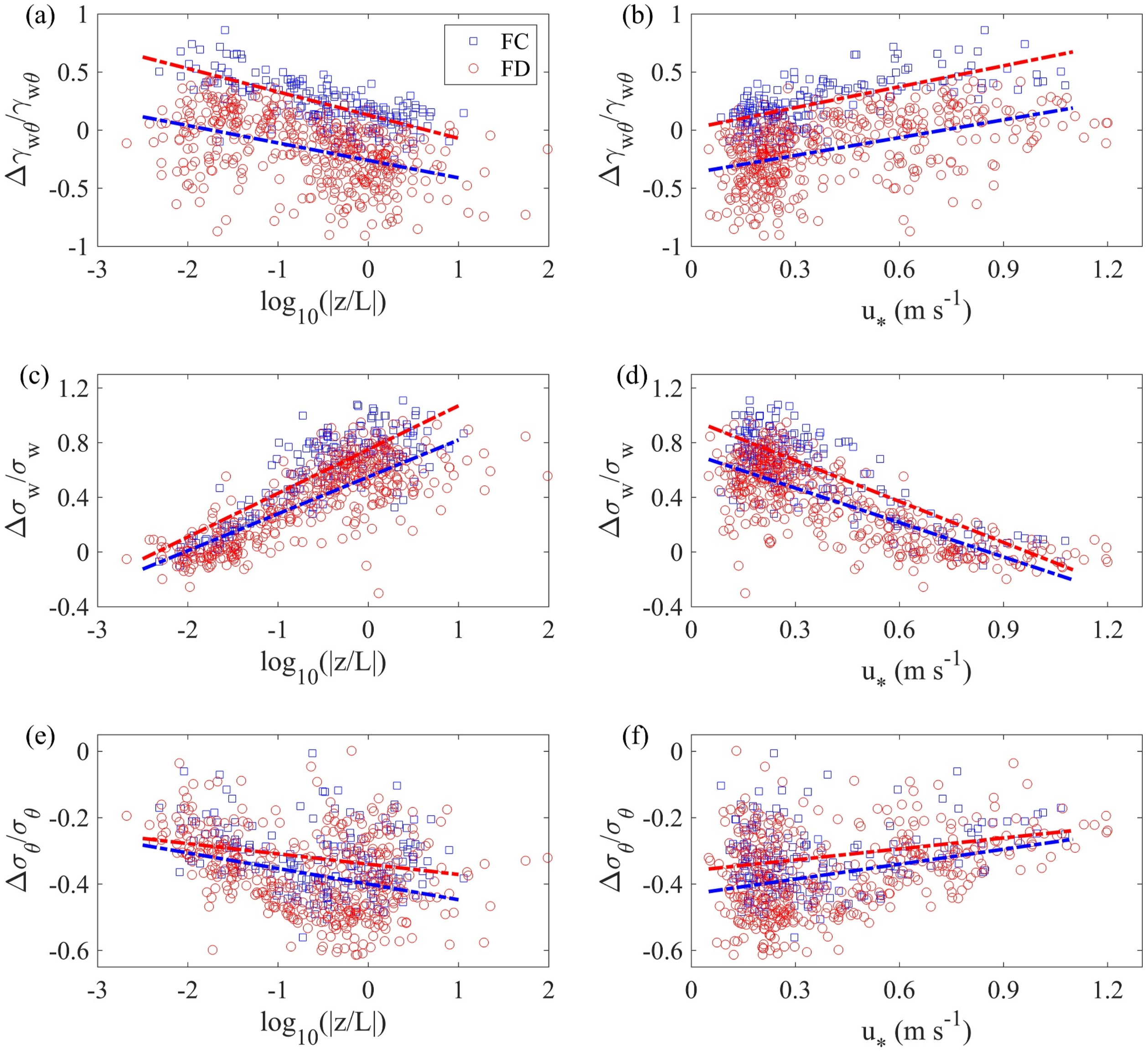

Figure 6. Relative changes in (a and b) transport efficiency $\left(\frac{\Delta\gamma_{w\theta}}{\gamma_{w\theta}}\right)$, (c and d) standard deviation for vertical velocity $\left(\frac{\Delta\sigma_w}{\sigma_w}\right)$, and (e and f) standard deviation for air temperature $\left(\frac{\Delta\sigma_\theta}{\sigma_\theta}\right)$ between 40.2 and 6.0 m with the (a, c, and e) stability parameter and (b, d, and f) friction velocity at 6.0 m. The data with values of $\frac{\Delta H}{H}$ larger than 0.1 are defined as flux convergence (FC), whereas the data with $\frac{\Delta H}{H}$ smaller than −0.1 are defined as flux divergence (FD). Note that the red and blue dashed lines denote the fitted linear relations for FC and FD, respectively.

correlation coefficient of two time series in time-frequency space. We select two 30-min intervals for further analysis, one for FC and one for FD, which we stress are highly representative of the respective conditions. The basic characteristics of the two selected intervals are presented in Table 1. It should be noted that the wind speeds at 40.2 and 6.0 m exhibit comparable values, which are commonly observed during unstable daytime conditions (Figure 2e).

Figures 7 and 8 show the temporal (x-axis) and scale (y-axis) distributions of the squared wavelet coherence of w' and θ' for the cases of FC and FD, respectively. Areas with high wavelet coherence (indicated by thick contours) are associated with turbulence structures with high correlation coefficients between w' and θ'. As the measurement height increases, the scale of highly correlated turbulence structures also increases, and all these areas demonstrate an in-phase relationship between w' and θ'. Figures 7 and 8 reveal a large number of turbulence structures with scales between 4 and 32 s at low levels (e.g., 6.0 m shown in Figures 7 and 8). The corresponding

Table 1
Characteristics of the Two Selected Intervals for FC and FD

	FC		FD	
	40.2 m	6.0 m	40.2 m	6.0 m
z/L	−0.85	−1.16	−0.79	−0.93
u_*	0.58	0.24	0.44	0.26
$\overline{w'\theta'}$	0.32	0.22	0.13	0.23
σ_w	0.96	0.47	0.72	0.41
σ_θ	0.54	0.83	0.61	1.00
$\gamma_{w\theta}$	0.62	0.56	0.30	0.56
Wind speed	1.67	1.51	1.22	1.25

length scales of these turbulence structures ranged from around 5.0 to 50.0 m for both cases of FC and FD at the height of 6.0 m. Here, the length scales of these turbulence structures are determined by multiplying their temporal scales with the associated wind speed in accordance with Taylor's hypothesis. However, at high levels (e.g., 40.2 m shown in Figure 7), the turbulence structures with smaller scales either merge into larger structures or vanish. Comparing Figure 8 with Figure 7, it is evident that turbulence structures with timescales ranging from 100 to 300 s are relatively less correlated for the FD case, leading to lower $\gamma_{w\theta}$ at higher levels (e.g., 40.2 m shown in Figure 8). These results are consistent with the previous studies (Z. Gao et al., 2016; Ruppert et al., 2006), which indicate that large eddies with time scales less than approximately 0.01 Hz often have negative contributions to fluxes and scalar similarity. The corresponding length scales of these large eddies range from 160 to 500 m and from 120 to 360 m for the cases of FC and FD, respectively, at the height of 40.2 m. These observed features further confirm the previous finding that large eddies are largely responsible for the FC and FD in the unstable ASL (Y. Zhang et al., 2010). In the case of FC, large eddies at high levels exhibit better correlation between w' and θ', thereby contributing more to H (Figure 9a). Conversely, in the case of FD, large eddies at high levels demonstrate poor correlation between w' and θ', resulting in reduced contribution to H (Figure 9b). One potential mechanical explanation is that, for FC, the atmospheric surface layer exhibits strong coupling with large eddies of w' and θ' showing high correlation, whereas for FD, the surface layer is relatively decoupled with large eddies of w' and θ' exhibiting lower correlation (Lan et al., 2018).

We now analyze the relative contributions of updrafts and downdrafts associated with large eddies to turbulent statistical quantities. Similar to the conditional sampling approach of quadrant analysis, updrafts can be understood as a composite of motions in the two quadrants characterized by positive w', whereas downdrafts can be attributed to a combination of motions in the two quadrants associated with negative w'. Here, updrafts (downdrafts) are defined as turbulent motions characterized by w' values exceeding one standard deviation of w' and being positively (negatively) oriented. Specifically, for each 30-min time series, w' and θ' were classified as updrafts when $w' > 0$ and $|w'| - \sigma_w > 0$ and as downdrafts when $w' < 0$ and $|w'| - \sigma_w < 0$. Their flux contribution (S) to $\overline{w'\theta'}$ and time durations (D) were calculated as

$$S(i) = \frac{1}{N}\int_0^N w'\theta' I_i(t)\,dt \Big/ \overline{w'\theta'}, \tag{6}$$

$$D(i) = \frac{1}{N}\int_0^N I_i(t)\,dt, \tag{7}$$

where $I_i(t) = 1$, when $w' > 0$ and $|w'| - \sigma_w > 0$ for updrafts, or when $w' < 0$ and $|w'| - \sigma_w < 0$ for downdrafts; otherwise, $I_i(t) = 0$. Figure 10 illustrates the distribution of the flux contributions and time durations of updrafts and downdrafts associated with large eddies of w' and θ' as well as their correlation coefficients at the heights of 40.2 and 6.0 m with respect to z/L. At 6.0 m, the flux contribution of the updrafts (downdrafts) first increases (decreases) as the instability increases and reaches its maximum (minimum) value around |z/L| = 0.1; whereas at 40.2 m, the flux contribution of the updrafts is about twice that of the downdrafts in the full range of atmospheric instability (left column in Figure 10). For the difference in flux contribution between updrafts and downdrafts (ΔS), FC at 40.2 m exhibits a slightly skewed probability density function (pdf) leaning toward the left (difference in peak location of 7%) as compared to FD (Figure 11a). In contrast, FC and FD at 6.0 m display a similar pdf distribution pattern (Figure 11b). Therefore, for FC, downdrafts have a relatively greater impact on H at 40.2 m compared to FD. As for the time duration, at 6.0 m, both D_{updrafts} and $D_{\text{downdrafts}}$ decrease from around 0.3 to 0.15 as instability increases, whereas at 40.2 m, the slope of decreasing trends for $D_{\text{downdrafts}}$ is greater than that for D_{updrafts} (middle column in Figure 10). For the difference in time duration between updrafts and downdrafts (ΔD), FC and FD at 40.2 m have a similar distribution pattern of pdf (Figure 11c). However, FC at 6.0 m displays a left-

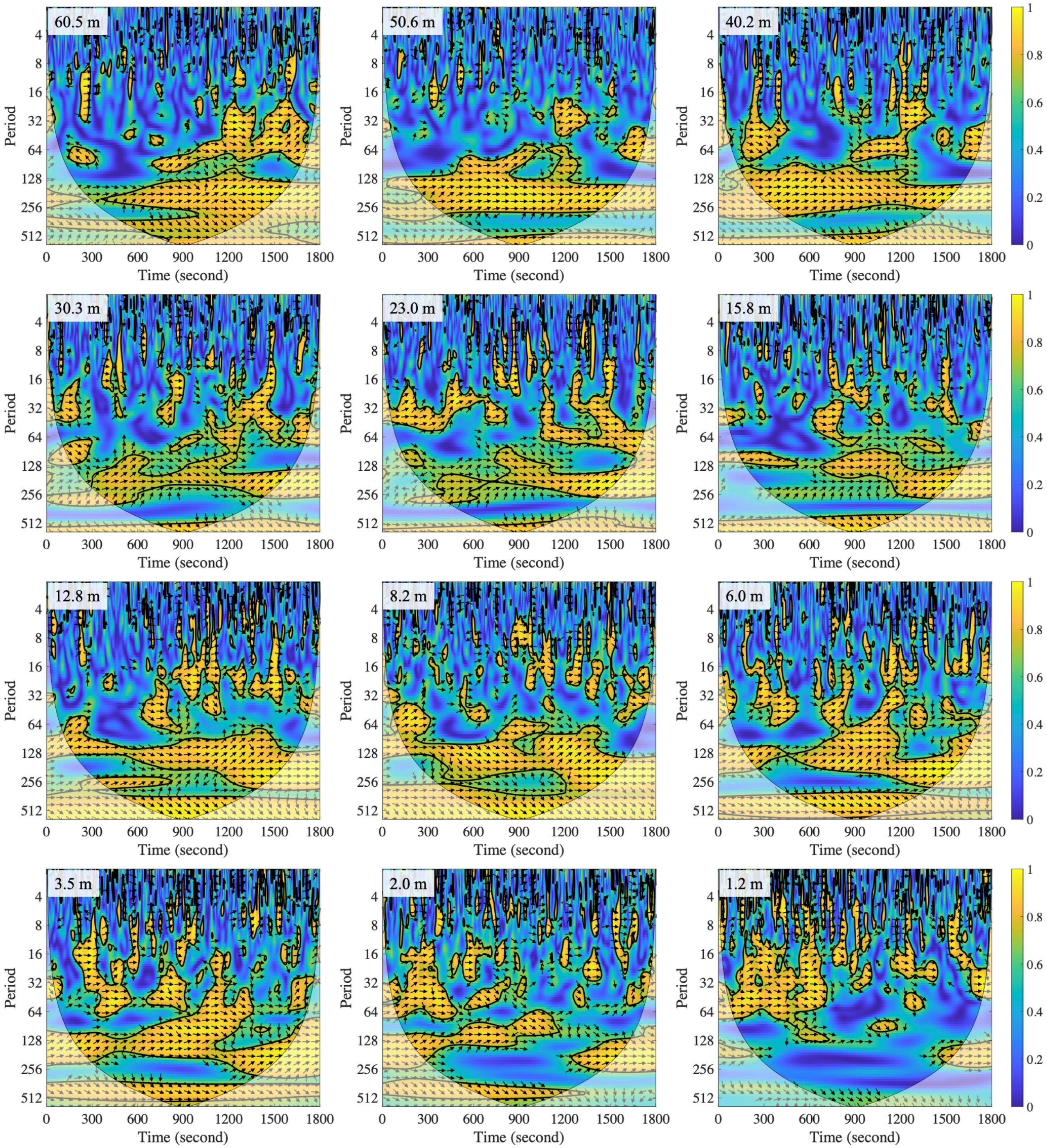

Figure 7. Squared wavelet coherence between 30-min time series of vertical velocity and sonic temperature measured at 12 heights for the selected case of FC. The thick black contours denote the 5% significance level against red noise. The cone of influence (COI) where edge effects might distort the picture is shown as a lighter shade. The relative phase relationship is shown as arrows (with in-phase pointing right, antiphase pointing left, and sonic temperature leading the vertical velocity by 90° pointing straight down).

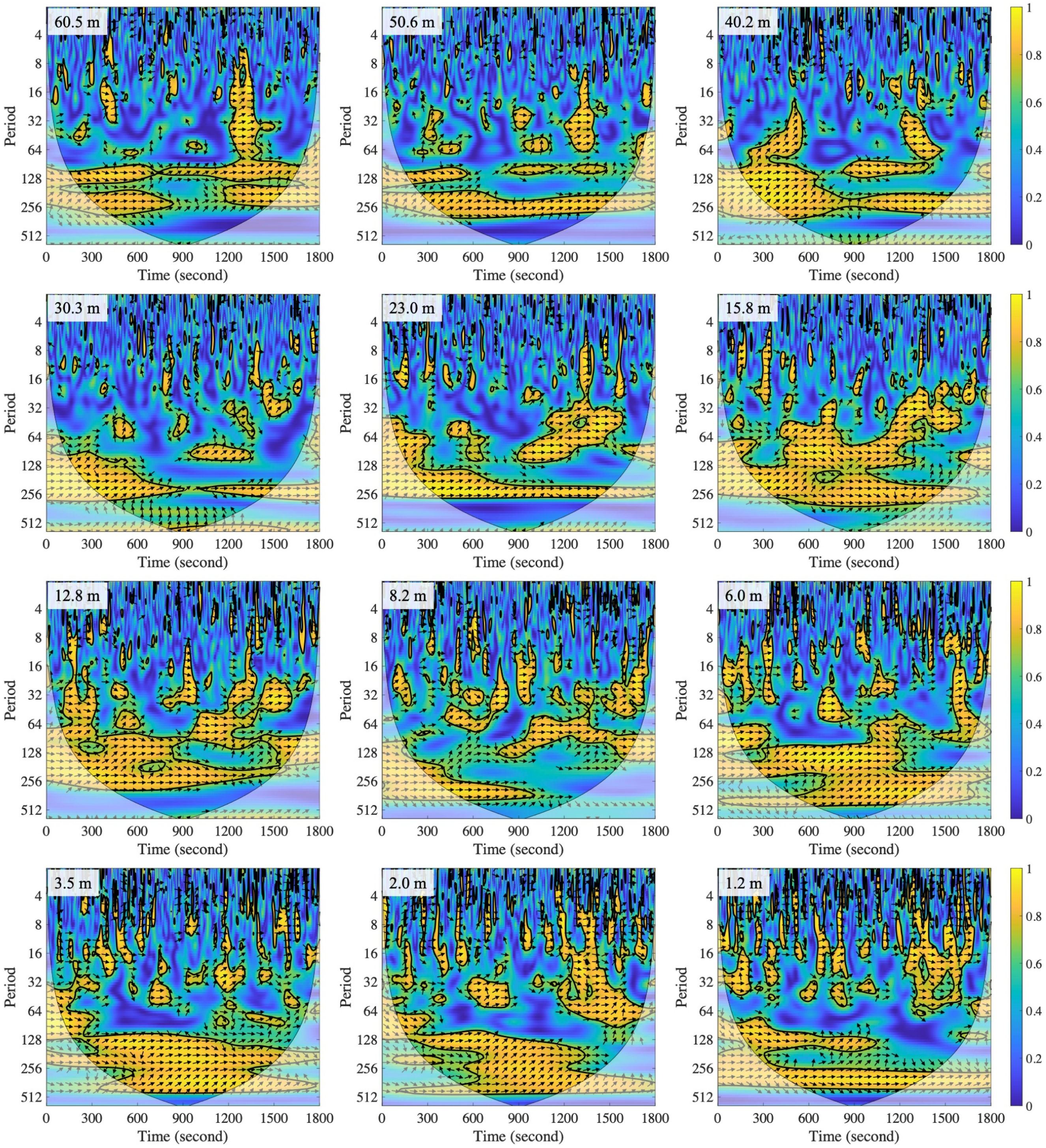

Figure 8. The same as in Figure 7, but for the time series of vertical velocity and sonic temperature measured at 12 heights for the selected case of FD.

skewed pdf compared to FD, indicating that relatively more downdrafts reach lower levels under flux convergence conditions (Figure 11d).

A notable difference is observed in the correlation coefficient of updrafts and downdrafts between FC and FD at 40.2 m. As the instability increases, $\gamma_{w\theta}$ of downdrafts gradually increases from 0.2 to 0.9 with larger values for FC compared to FD; whereas for updrafts, $\gamma_{w\theta}$ first increases rapidly from 0.4 to 0.8, then slowly from 0.8 to 0.9

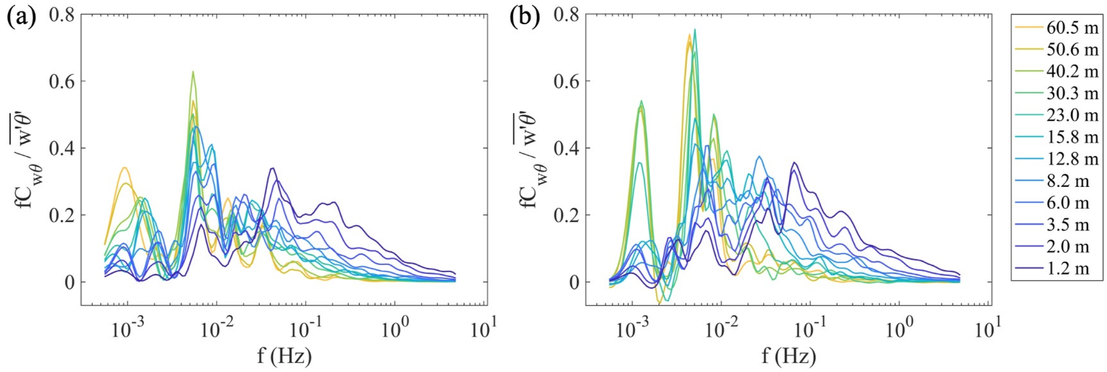

Figure 9. Normalized global wavelet cospectra of w-θ as a function of natural frequency f (Hz) at 12 heights for the two selected cases of (a) FC and (b) FD, respectively.

under strongly unstable conditions. These results suggest that in the downdrafts of large eddies, w' and θ' exhibit better synchronization for FC compared to FD, though w' and θ' in downdrafts are overall less synchronized to each other than those in updrafts. However, these difference in $\gamma_{w\theta}$ for downdrafts between FC and FD is not observed at the height of 6.0 m. It is also evident that at 40.2 m, the differences in $\gamma_{w\theta}$ between updrafts and downdrafts ($\Delta\gamma_{w\theta}$) for FC exhibit a left-skewed distribution compared to that for FD (Figure 11e; difference in peak location of 0.12). In contrast, at 6.0 m, the histogram of $\Delta\gamma_{w\theta}$ for FC displays a slightly right-skewed pattern compared to FD (Figure 11f; difference in peak location of 0.06). Overall, at 40.2 and 6.0 m, distinct patterns are observed in the characteristics of updrafts and downdrafts between FC and FD, especially in their flux contribution and transport efficiencies, rather than variances of w and θ (results not shown). These results suggest that at 40.2 m, downdrafts demonstrate more efficient flux transport for FC compared to FD; conversely, the opposite trend is observed at 6.0 m. Therefore, the observed flux convergence and divergence are primarily resulted from the combined effects of asymmetric transport of updrafts and downdrafts. The additional tests, based on the Kolmogorov-Smirnov test, reveal a statistically significant distinction at the 1% significance level between the two pdfs illustrated in Figures 11a, 11d, 11e, and 11f.

4. Conclusions

Using the turbulence data measured at 12 levels from 1.2 to 60.5 m above the ground over a semiarid ecosystem in the daytime unstable ASL, we examine the reasons behind the increased variability in the half-hourly sensible heat fluxes (H) with height. Generally, H exhibits larger point-to-point variations at higher levels than at lower levels, resulting in variations in FC and FD. However, H is underestimated at the bottom two levels (1.2 and 2.0 m) most-likely due to the influence of roughness sublayer; whereas at the top level (60.5 m), it is primarily due to the development of mixing layer during the morning hours. Therefore, we select the two heights of 40.2 and 6.0 m to further investigate the causes for FC and FD using the statistics at 6.0 m as references. The variations in H between 40.2 and 6.0 m are found to be closely associated with to changes in $\gamma_{w\theta}$.

To ensure the meaningfulness of the results, we classify the data as cases of FC when the relative changes in H between 40.2 and 6.0 m ($\Delta H/H$) > 10% and as cases of FD when $\Delta H/H < -10\%$, respectively. Approximately 25% and 55% of the selected runs are categorized into the FC and FD groups, respectively. Based on the classification, we conduct further analysis to examine the factors governing variations in $\gamma_{w\theta}$. Our results indicate that under unstable conditions of $|z/L| < 0.1$, when the vertical gradients in σ_w and σ_θ are constrained, FC is observed when $\gamma_{w\theta}$ at high levels is significantly larger than that at lower levels. However, as the gradients in σ_w further increases with enhanced instability, FC is observed even when $\gamma_{w\theta}$ at high levels is only slightly larger than that at lower levels.

We select two 30-min intervals to investigate the changes in turbulence structures associated with FC and FD. Our results suggest that large eddies play an important role in amplifying or attenuating the $\gamma_{w\theta}$ at higher levels compared to lower levels. Using conditional sampling to extract the updrafts and downdrafts of large eddies, distinct patterns are observed in the characteristics of updrafts and downdrafts between FC and FD at 40.2 and

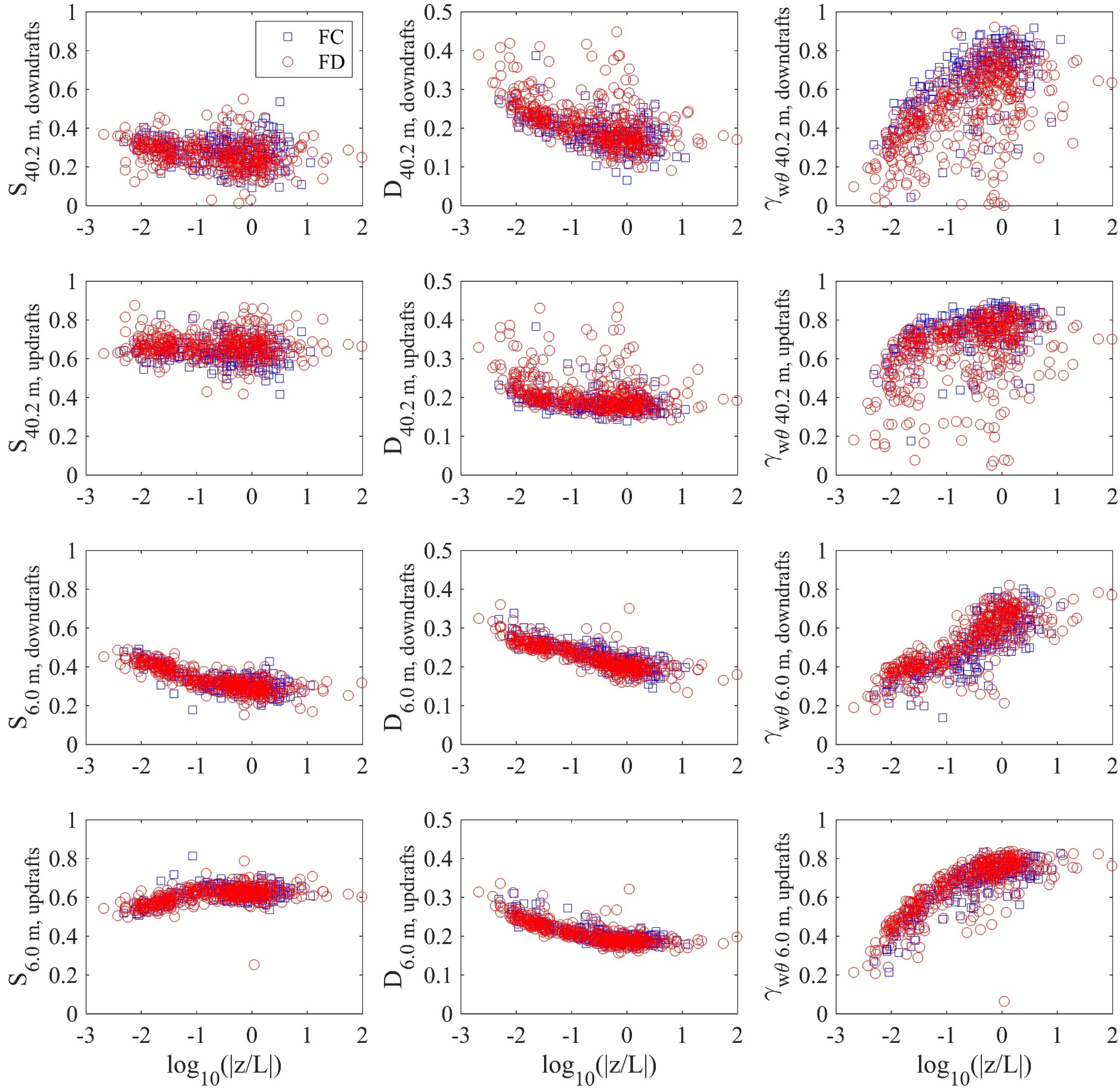

Figure 10. Distribution of (left column) $w'\theta'$ flux contribution (S), (middle column) $w'\theta'$ time duration (D), and (right column) correlation coefficients between w and θ with the stability parameter, for updrafts and downdrafts under flux convergence (FC) and divergence (FD) conditions at 40.2 and 6.0 m, respectively.

6.0 m, including differences in flux contribution, time duration, and transport efficiencies. Our results indicate that such changes in $\gamma_{w\theta}$ can be further linked to asymmetric flux transport by updrafts and downdrafts of large eddies. During daytime unstable conditions, the interaction between the ASL and the overlying convective boundary layer disrupts the stationarity of mean state of θ, potentially leading to flux convergence and divergence. This disruption limits the applicability of the MOST in the interpreting eddy covariance measurements. Our study highlights that the asymmetry is a main factor responsible for the departure of the observed turbulent fluxes from those described by MOST. Parameterizing such an asymmetry to improve MOST in predicting the ASL turbulent fluxes is thus a future research need.

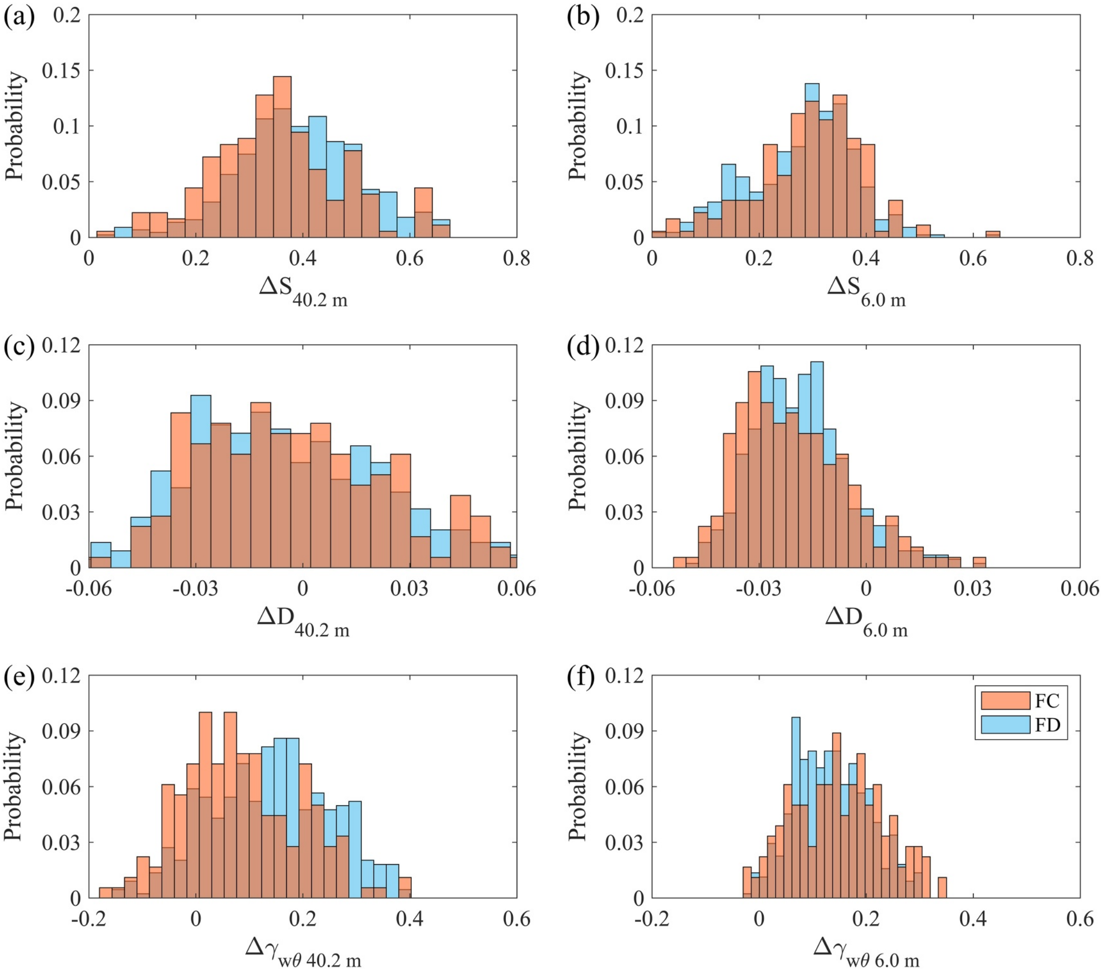

Figure 11. Histogram of probability of differences in (a and b) $w'\theta'$ flux contribution (ΔS), (c and d) $w'\theta'$ time duration (ΔD), and (e and f) correlation coefficients of w and θ $\left(\Delta\gamma_{w\theta}\right)$ between updrafts and downdrafts (e.g., $\Delta S_{40.2\ \mathrm{m}} = S_{40.2\ \mathrm{m\ updrafts}} - S_{40.2\ \mathrm{m\ downdrafts}}$) at (a, c, and e) 40.2 m and (b, d, and f) 6.0 m, respectively, for cases of flux convergence (FC) and divergence (FD).

Data Availability Statement

The data used in this study is publicly available from Z. Gao, Li, et al. (2024).

Acknowledgments

We thank Dan Li, Patrick O'Keeffe, Dennis Finn, Jason Rich, and Matthew S. Roetcisoender for their assistance in the lab and field. This work was supported by the National Key Research and Development Program of China (Grant 2023YFC3008002), the National Natural Science Foundation of China (Grants 42475087 and 42475077). H. Liu acknowledges support from NSF-AGS-2325687 and NSF-AGS-1853050.

References

Andreas, E. L. (1987). Spectral measurements in a disturbed boundary layer over snow. *Journal of the Atmospheric Sciences*, *44*(15), 1912–1939. https://doi.org/10.1175/1520-0469(1987)044<1912:SMIADB>2.0.CO;2

Barthlott, C., Drobinski, P., Fesquet, C., Dubos, T., & Pietras, C. (2007). Long-term study of coherent structures in the atmospheric surface layer. *Boundary-Layer Meteorology*, *125*(1), 1–24. https://doi.org/10.1007/s10546-007-9190-9

Charuchittipan, D., Babel, W., Mauder, M., Leps, J.-P. P., & Foken, T. (2014). Extension of the averaging time in eddy-covariance measurements and its effect on the energy balance closure. *Boundary-Layer Meteorology*, *152*(3), 303–327. https://doi.org/10.1007/s10546-014-9922-6

Detto, M., & Katul, G. G. (2007). Simplified expressions for adjusting higher-order turbulent statistics obtained from open path gas analyzers. *Boundary-Layer Meteorology*, *122*(1), 205–216. https://doi.org/10.1007/s10546-006-9105-1

Dupont, S., & Patton, E. G. (2012). Momentum and scalar transport within a vegetation canopy following atmospheric stability and seasonal canopy changes: The CHATS experiment. *Atmospheric Chemistry and Physics*, *12*(13), 5913–5935. https://doi.org/10.5194/acp-12-5913-2012

Eder, F., De Roo, F., Rotenberg, E., Yakir, D., Schmid, H. P., & Mauder, M. (2015). Secondary circulations at a solitary forest surrounded by semi-arid shrubland and their impact on eddy-covariance measurements. *Agricultural and Forest Meteorology*, *211–212*, 115–127. https://doi.org/10.1016/j.agrformet.2015.06.001

Farge, M. (1992). Wavelet transforms and their applications to turbulence. *Annual Review of Fluid Mechanics*, *24*(1), 395–458. https://doi.org/10.1146/annurev.fl.24.010192.002143

Finn, D., Carter, R. G., Eckman, R. M., Rich, J. D., Gao, Z., & Liu, H. (2018). Plume dispersion in low-wind-speed conditions during Project Sagebrush Phase 2, with emphasis on concentration variability. *Boundary-Layer Meteorology*, *169*(1), 67–91. https://doi.org/10.1007/s10546-018-0360-8

Finn, D., Clawson, K. L., Eckman, R. M., Liu, H., Russell, E. S., Gao, Z., & Brooks, S. (2016). Project sagebrush: Revisiting the value of the horizontal plume spread parameter σy. *Journal of Applied Meteorology and Climatology*, *55*(6), 1305–1322. https://doi.org/10.1175/JAMC-D-15-0283.1

Foken, T. (2008). The energy balance closure problem: An overview. *Ecological Applications*, *18*(6), 1351–1367. https://doi.org/10.1890/06-0922.1

Gao, W., & Li, B. L. (1993). Wavelet analysis of coherent structures at the atmosphere-forest interface. *Journal of Applied Meteorology*, *32*(11), 1717–1725. https://doi.org/10.1175/1520-0450(1993)032%3C1717:WAOCSA%3E2.0.CO

Gao, Z., Li, L., Liu, H., Li, D., & Yang, B. (2024). Flux convergence and divergence linked to asymmetric transport by large turbulent eddies in the unstable atmospheric surface layer [Dataset]. *Zenodo*. https://doi.org/10.5281/zenodo.10674143

Gao, Z., Liu, H., Arntzen, E., Mcfarland, D. P., Chen, X., & Huang, M. (2020). Uncertainties in turbulent statistics and fluxes of CO_2 associated with density effect corrections. *Geophysical Research Letters*, *47*(15). https://doi.org/10.1029/2020GL088859

Gao, Z., Liu, H., Katul, G. G., & Foken, T. (2017). Non-closure of the surface energy balance explained by phase difference between vertical velocity and scalars of large atmospheric eddies. *Environmental Research Letters*, *12*(3), 034025. https://doi.org/10.1088/1748-9326/aa625b

Gao, Z., Liu, H., Li, D., Yang, B., Walden, V., Li, L., & Bogoev, I. (2024). Uncertainties in temperature statistics and fluxes determined by sonic anemometers due to wind-induced vibrations of mounting arms. *Atmospheric Measurement Techniques*, *17*(13), 4109–4120. https://doi.org/10.5194/amt-17-4109-2024

Gao, Z., Liu, H., Russell, E. S., Huang, J., Foken, T., & Oncley, S. P. (2016). Large eddies modulating flux convergence and divergence in a disturbed unstable atmospheric surface layer. *Journal of Geophysical Research*, *121*(4), 1475–1492. https://doi.org/10.1002/2015JD024529

Grinsted, A., Moore, J. C., & Jevrejeva, S. (2004). Application of the cross wavelet transform and wavelet coherence to geophysical time series. *Nonlinear Processes in Geophysics*, *11*(5/6), 561–566. https://doi.org/10.5194/NPG-11-561-2004

Högström, U. (1990). Analysis of turbulence structure in the surface layer with a modified similarity formulation for near neutral conditions. *Journal of the Atmospheric Sciences*, *47*(16), 1949–1972. https://doi.org/10.1175/1520-0469(1990)047%3C1949:AOTSIT%3E2.0.CO

Hudgins, L., Friehe, C. A., & Mayer, M. E. (1993). Wavelet transforms and atmospheric turbulence. *Physical Review Letters*, *71*(20), 3279–3282. https://doi.org/10.1103/PhysRevLett.71.3279

Katul, G. G., Kuhn, G., Schieldge, J., & Hsieh, C.-I. (1997). The ejection-sweep character of scalar fluxes in the unstable surface layer. *Boundary-Layer Meteorology*, *83*(1), 1–26. https://doi.org/10.1023/A:1000293516830

Katul, G. G., Lai, C.-T., Schäfer, K., Vidakovic, B., Albertson, J., Ellsworth, D., & Oren, R. (2001). Multiscale analysis of vegetation surface fluxes: From seconds to years. *Advances in Water Resources*, *24*(9–10), 1119–1132. https://doi.org/10.1016/S0309-1708(01)00029-X

Lan, C., Liu, H., Li, D., Katul, G. G., & Finn, D. (2018). Distinct turbulence structures in stably stratified boundary layers with weak and strong surface shear. *Journal of Geophysical Research: Atmospheres*, *123*(15), 7839–7854. https://doi.org/10.1029/2018JD028628

Li, D., & Bou-Zeid, E. (2011). Coherent structures and the dissimilarity of turbulent transport of momentum and scalars in the unstable atmospheric surface layer. *Boundary-Layer Meteorology*, *140*(2), 243–262. https://doi.org/10.1007/s10546-011-9613-5

Li, D., Katul, G. G., & Liu, H. (2018). Intrinsic constraints on asymmetric turbulent transport of scalars within the constant flux layer of the lower atmosphere. *Geophysical Research Letters*, *45*(4), 2022–2030. https://doi.org/10.1002/2018GL077021

Li, Q., Gentine, P., Mellado, J. P., & Mccoll, K. A. (2018). Implications of nonlocal transport and conditionally averaged statistics on Monin-Obukhov similarity theory and Townsend's attached eddy hypothesis. *Journal of the Atmospheric Sciences*, *75*(10), 3403–3431. https://doi.org/10.1175/JAS-D-17-0301.1

Liu, H., Gao, Z., & Katul, G. G. (2021). Non-closure of surface energy balance linked to asymmetric turbulent transport of scalars by large eddies. *Journal of Geophysical Research: Atmospheres*, *126*(7), e2020JD034474. https://doi.org/10.1029/2020JD034474

Liu, H., Peters, G., & Foken, T. (2001). New equations for sonic temperature variance and buoyancy heat flux with an omnidirectional sonic anemometer. *Boundary-Layer Meteorology*, *100*(3), 459–468. https://doi.org/10.1023/A:1019207031397

Mauder, M., Oncley, S. P., Vogt, R., Weidinger, T., Ribeiro, L., Bernhofer, C., et al. (2007). The energy balance experiment EBEX-2000. Part II: Intercomparison of eddy-covariance sensors and post-field data processing methods. *Boundary-Layer Meteorology*, *123*(1), 29–54. https://doi.org/10.1007/s10546-006-9139-4

McNaughton, K. G., & Laubach, J. (2000). Power spectra and cospectra for wind and scalars in a disturbed surface layer at the base of an advective inversion. *Boundary-Layer Meteorology*, *96*(1–2), 143–185. https://doi.org/10.1023/A%3A1002477120507

Ruppert, J., Thomas, C., & Foken, T. (2006). Scalar similarity for relaxed eddy accumulation methods. *Boundary-Layer Meteorology*, *120*(1), 39–63. https://doi.org/10.1007/s10546-005-9043-3

Schotanus, P., Nieuwstadt, F. T. M., & De Bruin, H. A. R. (1983). Temperature measurement with a sonic anemometer and its application to heat and moisture fluxes. *Boundary-Layer Meteorology*, *26*(1), 81–93. https://doi.org/10.1007/BF00164332

Smedman, A.-S., Högström, U., Hunt, J. C. R., & Sahlée, E. (2007). Heat/mass transfer in the slightly unstable atmospheric surface layer. *Quarterly Journal of the Royal Meteorological Society*, *133*(622), 37–51. https://doi.org/10.1002/qj.7

Steiner, A. L., Pressley, S. N., Botros, A., Jones, E., Chung, S. H., & Edburg, S. L. (2011). Analysis of coherent structures and atmosphere-canopy coupling strength during the CABINEX field campaign. *Atmospheric Chemistry and Physics*, *11*(23), 11921–11936. https://doi.org/10.5194/acp-11-11921-2011

Stoy, P. C., Mauder, M., Foken, T., Marcolla, B., Boegh, E., Ibrom, A., et al. (2013). A data-driven analysis of energy balance closure across FLUXNET research sites: The role of landscape scale heterogeneity. *Agricultural and Forest Meteorology*, *171–172*, 137–152. https://doi.org/10.1016/j.agrformet.2012.11.004

Stull, R. B. (1988). *An introduction to boundary layer meteorology*. Kluwer Academic Publishers. https://doi.org/10.1007/978-94-009-3027-8

Sun, J., Lenschow, D. H., LeMone, M. A., & Mahrt, L. (2016). The role of large-coherent-eddy transport in the atmospheric surface layer based on CASES-99 observations. *Boundary-Layer Meteorology*, *160*(1), 83–111. https://doi.org/10.1007/s10546-016-0134-0

Thomas, C., & Foken, T. (2007). Organised motion in a tall spruce canopy: Temporal scales, structure spacing and terrain effects. *Boundary-Layer Meteorology*, *122*(1), 123–147. https://doi.org/10.1007/s10546-006-9087-z

Vickers, D., & Mahrt, L. (1997). Quality control and flux sampling problems for tower and aircraft data. *Journal of Atmospheric and Oceanic Technology*, *14*(3), 512–526. https://doi.org/10.1175/1520-0426(1997)014%3C0512:QCAFSP%3E2.0.CO

Wang, G., Huang, J., Guo, W., Zuo, J., Wang, J., Bi, J., et al. (2010). Observation analysis of land-atmosphere interactions over the Loess Plateau of northwest China. *Journal of Geophysical Research*, *115*(D00K17). https://doi.org/10.1029/2009JD013372

Wang, L., Li, D., Gao, Z., Sun, T., Guo, X., & Bou-Zeid, E. (2014). Turbulent transport of momentum and scalars above an urban canopy. *Boundary-Layer Meteorology*, *150*(3), 485–511. https://doi.org/10.1007/s10546-013-9877-z

Webb, E. K., Pearman, G. I., & Leuning, R. (1980). Correction of flux measurements for density effects due to heat and water vapour transfer. *Quarterly Journal of the Royal Meteorological Society*, *106*(447), 85–100. https://doi.org/10.1002/qj.49710644707

Wilczak, J. M., Oncley, S. P., & Stage, S. A. (2001). Sonic anemometer tilt correction algorithms. *Boundary-Layer Meteorology*, *99*(1), 127–150. https://doi.org/10.1023/A:1018966204465

Yao, J., Liu, H., Huang, J., Gao, Z., Wang, G., Li, D., et al. (2020). Accelerated dryland expansion regulates future variability in dryland gross primary production. *Nature Communications*, *11*(1), 1665. https://doi.org/10.1038/s41467-020-15515-2

Zhang, L., Zhang, H., Zhang, X., Li, Q., Wu, B., Cai, X., et al. (2023). Dissimilarity of turbulent transport of momentum and heat under unstable conditions linked to convective circulations. *Journal of Geophysical Research: Atmospheres*, *128*(8), e2022JD037997. https://doi.org/10.1029/2022JD037997

Zhang, Y., Liu, H., Foken, T., Williams, Q., Liu, S., Mauder, M., & Liebethal, C. (2010). Turbulence spectra and cospectra under the influence of large eddies in the Energy Balance EXperiment (EBEX). *Boundary-Layer Meteorology*, *136*(2), 235–251. https://doi.org/10.1007/s10546-010-9504-1

Zhang, Y., Liu, H., Foken, T., Williams, Q., Mauder, M., & Thomas, C. (2011). Coherent structures and flux contribution over an inhomogeneously irrigated cotton field. *Theoretical and Applied Climatology*, *103*(1–2), 119–131. https://doi.org/10.1007/s00704-010-0287-6

Zhou, Y., Li, D., Liu, H., & Li, X. (2018). Diurnal variations of the flux imbalance over homogeneous and heterogeneous landscapes. *Boundary-Layer Meteorology*, *168*(3), 1–26. https://doi.org/10.1007/s10546-018-0358-2